



On the structures and bonding of copper boride nanoclusters, Cu_2B_x^- ($x = 5-7$)

Anton S. Pozdeev^{a,1}, Wei-Jia Chen^{b,1}, Maksim Kulichenko^c, Hyun Wook Choi^b, Alexander I. Boldyrev^a, Lai-Sheng Wang^{b,*}

^a Department of Chemistry and Biochemistry, Utah State University, Logan, UT, 84322, United States

^b Department of Chemistry, Brown University, Providence, RI, 02912, United States

^c Theoretical Division, Los Alamos National Laboratory, Los Alamos, NM, 87545, United States

ARTICLE INFO

Keywords:

Copper boride clusters
Boron clusters
Photoelectron spectroscopy
Chemical bonding
Computational chemistry
Borophene

ABSTRACT

Borophenes, a new class of synthetic 2D nanomaterials, are usually grown on coinage metal surfaces because of the weak boron-metal bonding. Coinage metal and boron binary clusters provide ideal systems to examine the bonding and interactions between coinage metals and boron, which are important to understand and control the growth of borophenes. Here we report a photoelectron spectroscopy and quantum chemical investigation on a series of di-copper boride clusters, Cu_2B_x^- ($x = 5-7$). Vibrationally resolved photoelectron spectra are measured for the binary copper-boron clusters and are combined with quantum calculations to probe their structures and bonding. We find that all three clusters exhibit elongated ribbon-like structures consisting of a double-chain B_x motif and two terminal Cu-B covalent bonds, similar to the corresponding di-hydride (H_2B_x^-) and di-auride (Au_2B_x^-) clusters. The surprising covalent bonds between Cu and boron in these clusters are shown to be dictated by the high stability of the double-chain B_x motifs in this size range, whereas ionic bonding between Cu and boron is expected to take place in larger boron motifs.

1. Introduction

Boron forms a variety of bulk allotropes consisting of different cage structures due to its electron deficiency [1–3]. However, there is no boron allotrope with a graphite-like layered structure consisting of hexagonal units. Density function theory (DFT) calculations suggested that a planar boron monolayer could be formed out of a triangular boron lattice with hexagonal vacancies [4,5]. Different from bulk boron, size-selected boron clusters have been found to possess planar structures through joint experimental and theoretical studies, in particular, photoelectron spectroscopy (PES) [6–11]. Planar boron clusters usually consist of B_3 triangles interspersed with tetragonal, pentagonal or hexagonal vacancies [8–10,12–16]. The structures of planar boron clusters are stabilized by two-center two-electron (2c-2e) B–B σ bonds on the periphery and delocalized $nc-2e$ σ and π bonds over the plane of the clusters [17–19]. The discovery of the C_{6v} B_{36}^- cluster with a central hexagonal vacancy provided the first experimental evidence for a graphene-like boron sheet (borophene) [20]. The B_{35}^- cluster was further

found to possess a planar structure with a double hexagonal vacancy, a more flexible building block for borophenes [21]. Subsequently, borophenes were successfully synthesized on metal substrates [22,23], becoming a new class of synthetic 2D materials with novel properties [24,25]. The discovery of the B_{40} cage cluster marks the first all-boron fullerene (borospherene) [26]. Even though B_{80} was first suggested to have a fullerene-like cage structure [27], further calculations showed that the cage structure was a much higher energy isomer [28,29]. Recently, the B_{48}^- cluster has been found to be the first bilayer boron clusters [30,31], laying the foundation for bilayer borophenes which have also been synthesized subsequently on coinage metal substrates [32,33]. Theoretical analyses revealed that charge transfer from the Cu substrate to the first layer of boron played an important role in the stabilization of the second layer of borophene [32]. Thus, it is essential to investigate the interactions between boron and the metal substrate at the atomic level, in order to understand and control the growth of borophene materials.

There has been significant research on metal-doped boron clusters to

* Corresponding author.

E-mail address: lai-sheng_wang@brown.edu (L.-S. Wang).

¹ The authors contribute equally to this work.

study the interactions between metal atoms and boron motifs over the last two decades using PES and computational chemistry [10,34,35]. Investigations on transition-metal-doped boron clusters revealed a wide variety of structures including metal-centered molecular wheels [36–38], metallo-boronanotubes [39–41], and metallo-borophenes [34, 42,43]. For small boron clusters, B_7^- , B_8^- , and B_9^- were found to possess interesting planar structures consisting of a central B atom coordinated hyper-valently by a monocyclic boron ring [17,44]. The closed-shell B_9^- cluster has a highly symmetric D_{8h} structure with σ and π double aromaticity [17,45], which inspired the design and discovery of a series of metal-centered borometallic molecular wheels [36–38]. The closed-shell B_7^{3-} and B_8^{2-} species, which are also doubly aromatic, were found in various metal-doped boron clusters and even boron oxide clusters due to their high stability derived from double aromaticity [46–49]. More interestingly, the structure and bonding in B_7^{3-} , B_8^{2-} , B_9^- were found to be similar to that in the prototypical hydrocarbons $C_5H_5^-$, C_6H_6 and $C_7H_7^-$ in a recent investigation on a series of LnB_8 lanthanide clusters, leading to the proposal of “borozene” for this series of wheel-like boron clusters [50]. Recent studies on BiB_8^- and AuB_8^- provided new examples for the high stability of borozenes [51,52].

On the other hand, multi-metal boron clusters or coinage boron clusters have been less explored. Di-lanthanide boron clusters $Ln_2B_x^-$ ($x = 7–9$) were found to have inverse-sandwich structures with a monocyclic boron ring [53,54], whereas di-gold $Au_2B_x^{0/-}$ ($x = 3,6,7$) and di-bismuth $Bi_2B_x^{0/-}$ ($x = 2–4$) species were found to consist of double-chain boron motifs with two terminal metal atoms [55–58]. A theoretical study on di-phosphorus boron clusters found similar double-chain structures [59]. Di-tantalum boron clusters $Ta_2B_x^-$ ($x = 2–5$) were shown to contain a Ta_2 dimer surrounded by boron atoms [60], leading to the highly symmetric inverse sandwich D_{6h} $Ta_2B_6^-$ [61]. Theoretical studies suggested that several other transition metal M_2B_8 clusters may also have inverse-sandwich-type structures [35], while M_2B_8 ($M = Mg, Zn, Cd, \text{ and } Hg$) species were predicted to be M_2 -borozene complexes [62–64]. Our recent study on $Cu_2B_8^-$ showed a unique structure consisting of a Cu_2^+ dimer interacting with the B_8^{2-} borozene [65]. The Cu–Cu bond length is similar to that of bare Cu_2^+ and further bonding analyses revealed that $Cu_2B_8^-$ can be viewed as a Cu_2^+ -borozene complex, the charge transfer from copper to boron in $Cu_2B_8^-$ is similar to that in the growth of bilayer borophene on copper substrate, where charge transfer from the copper substrate to the first layer of borophene is critical to stabilize the structure [32].

Copper-boron binary clusters ($Cu_xB_y^-$) are ideal models to understand the interaction between boron and copper. In the current work, we report a joint PES and quantum chemical study on the $Cu_2B_x^-$ ($x = 5–7$) clusters. Well-resolved photoelectron spectra are obtained at different detachment photon energies and are used to compare with theoretical results to investigate the structures and bonding of the di-copper boron clusters. Different from $Cu_2B_8^-$, these smaller clusters all possess structures consisting of a double-chain boron motif with one copper atom covalently bonded to a boron atom on each end at the apex positions, similar to what has been observed previously in the corresponding digold boron clusters [55,56].

2. Experimental and theoretical methods

2.1. Experimental method

The experiment was carried out using a PES apparatus equipped with a laser vaporization cluster source, a time-of-flight (TOF) mass spectrometer, and a magnetic-bottle photoelectron analyzer, details of which can be found elsewhere [9,66]. The $Cu_2B_x^-$ clusters were produced by laser vaporization of a hot-pressed $Cu/^{11}B$ disk target prepared using natural isotopic Cu powder and 97% ^{11}B -enriched boron powder. The clusters formed inside a large-waiting-room nozzle were entrained by a He carrier gas seeded with 5% Ar and underwent a supersonic expansion. After passing through a skimmer, negatively charged clusters from

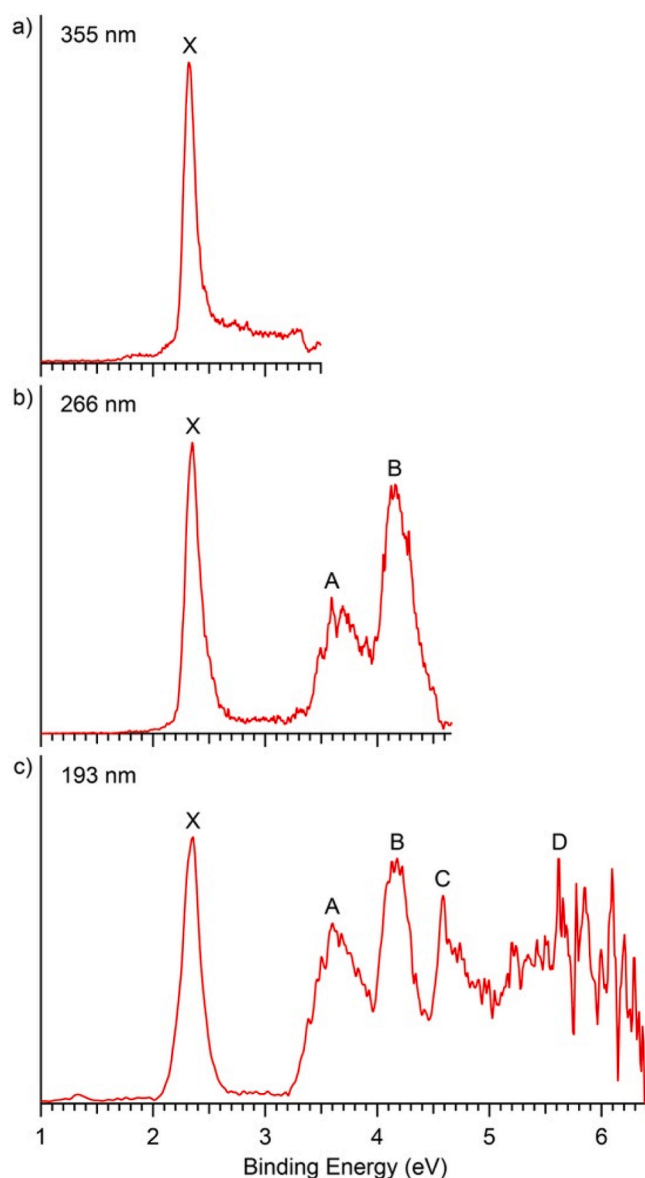


Fig. 1. The photoelectron spectra of $Cu_2B_5^-$ at (a) 355 nm (3.496 eV), (b) 266 nm (4.661 eV), and (c) 193 nm (6.424 eV).

the collimated beam were extracted perpendicularly into the TOF mass spectrometer. The $Cu_2B_x^-$ ($x = 5–7$) clusters of interest were mass-selected and decelerated before photodetachment. Three different photon energies were used in the experiment: 355 nm (3.496 eV) and 266 nm (4.661 eV) from a Nd:YAG laser, and 193 nm (6.424 eV) from an ArF excimer laser. Photoelectrons were collected by the magnetic bottle and analyzed using a 3.5-m-long TOF tube. The photoelectron kinetic energies were calibrated using the known transitions of the Bi^- atomic anion. The kinetic energy (E_k) resolution ($\Delta E_k/E_k$) of our PES apparatus was around 2.5%, i.e., ~ 25 meV for electrons with 1 eV kinetic energy.

2.2. Theoretical method

Global minimum (GM) searches were performed by using the AFFCK global optimization method [67]. At least 1000 random structures were generated for each stoichiometry. Both singlet and triplet states for structures with an even number of electrons, doublet and quartet states for structures with an odd number of electrons were tested for each cluster. The generated structures were initially optimized at the PBE0/LANL2DZ level of theory [68,69] with the Hay-Wadt

Table 1

The measured VDEs of Cu_2B_5^- compared with theoretical results of the GM structure at the PBE0/aug-cc-pVTZ level of theory. All energies are in eV.

	Final state and electron configuration	VDE (exp) ^a	VDE (theo)
X	${}^2\text{A} \{ \dots (10b)^2(11a)^2(12a)^2(11b)^2(12b)^2(13a)^2(13b)^2(14a)^1 \}$	2.32	2.15
A	${}^2\text{B} \{ \dots (10b)^2(11a)^2(12a)^2(11b)^2(12b)^2(13a)^2(13b)^1(14a)^2 \}$	3.59	3.60
B	${}^2\text{A} \{ \dots (10b)^2(11a)^2(12a)^2(11b)^2(12b)^2(13a)^1(13b)^2(14a)^2 \}$	4.15	4.13
	${}^2\text{B} \{ \dots (10b)^2(11a)^2(12a)^2(11b)^2(12b)^1(13a)^2(13b)^2(14a)^2 \}$		4.21
C	${}^2\text{B} \{ \dots (10b)^2(11a)^2(12a)^2(11b)^2(12b)^2(13a)^2(13b)^2(14a)^2 \}$	4.59	4.56
	${}^2\text{A} \{ \dots (10b)^2(11a)^2(12a)^1(11b)^2(12b)^2(13a)^2(13b)^2(14a)^2 \}$		4.7
D	${}^2\text{A} \{ \dots (10b)^2(11a)^1(12a)^2(11b)^2(12b)^2(13a)^2(13b)^2(14a)^2 \}$	~5.6	5.3
	${}^2\text{B} \{ \dots (10b)^1(11a)^2(12a)^2(11b)^2(12b)^2(13a)^2(13b)^2(14a)^2 \}$		5.3

^a The uncertainty of the VDEs was ± 0.02 eV.

pseudopotential applied to the Cu atoms [70]. Then, low-lying isomers were reoptimized and harmonic frequencies were calculated at the PBE0/aug-cc-pVTZ level of theory [71,72], as implemented in Gaussian-16 [73]. All low-lying isomers within the energy range of 10–15 kcal/mol above the GM were ordered according to energies obtained at the CCSD(T)/aug-cc-pVTZ//PBE0/aug-cc-pVTZ level of theory with zero-point energy correction for each stoichiometry. The one-determinant character of the GM wave functions was examined by the wave function stability test (stable = opt) [74].

The first vertical detachment energy (VDE₁) was calculated as the energy difference between a neutral and the corresponding anion both at the anion geometry optimized at the CCSD(T)/aug-cc-pVTZ level of theory. Higher VDEs for the GM structure and some low-lying isomers were calculated by using two approaches: (1) time-dependent DFT (TD-DFT) at the PBE0/aug-cc-pVTZ level of theory, and (2) Δ CCSD(T)/aug-cc-pVTZ. The adiabatic detachment energy (ADE) for the GM structure was calculated as the energy difference between the optimized anion and the optimized neutral structure started from the corresponding anion. Although spin-orbit effects were not treated explicitly in the present work, the good agreement between the theoretical VDEs with the experimental spectra, as well as previous works that used similar algorithms [51,65] allowed us to justify the chosen approach.

Chemical bonding was analyzed using the Adaptive Natural Density Partitioning (AdNDP) algorithm implemented in AdNDP 2.0 as a time-proven probe for deciphering delocalized bonding in complex clusters [75,76]. This method is based on the idea that an electron pair is the main element of chemical bonding models. The AdNDP algorithm recovers both classical Lewis bonds (i.e., 1c-2e lone-pairs and 2c-2e bonds) and delocalized bonds. The latter naturally introduces the concepts of aromaticity and antiaromaticity [77]. In the current work, the AdNDP analyses were done at the PBE0/aug-cc-pVTZ level of theory.

3. Experimental and theoretical results

3.1. Experimental results

The photoelectron spectra of Cu_2B_x^- were measured at three wavelengths, as shown in Fig. 1–3 for $x = 5–7$, respectively. From the single-particle approximation, the detachment features (labeled as X, A, B, ...) come from electron detachment from valence molecular orbitals (MOs) of the GM structure of each Cu_2B_x^- cluster and the binding energies observed represent the negative of the orbital energies based on the Koopmans' theorem. Spectroscopically, these features represent electron detachment transitions from the ground state of the anion to the ground (X) and excited (A, B, ...) states of the corresponding neutral

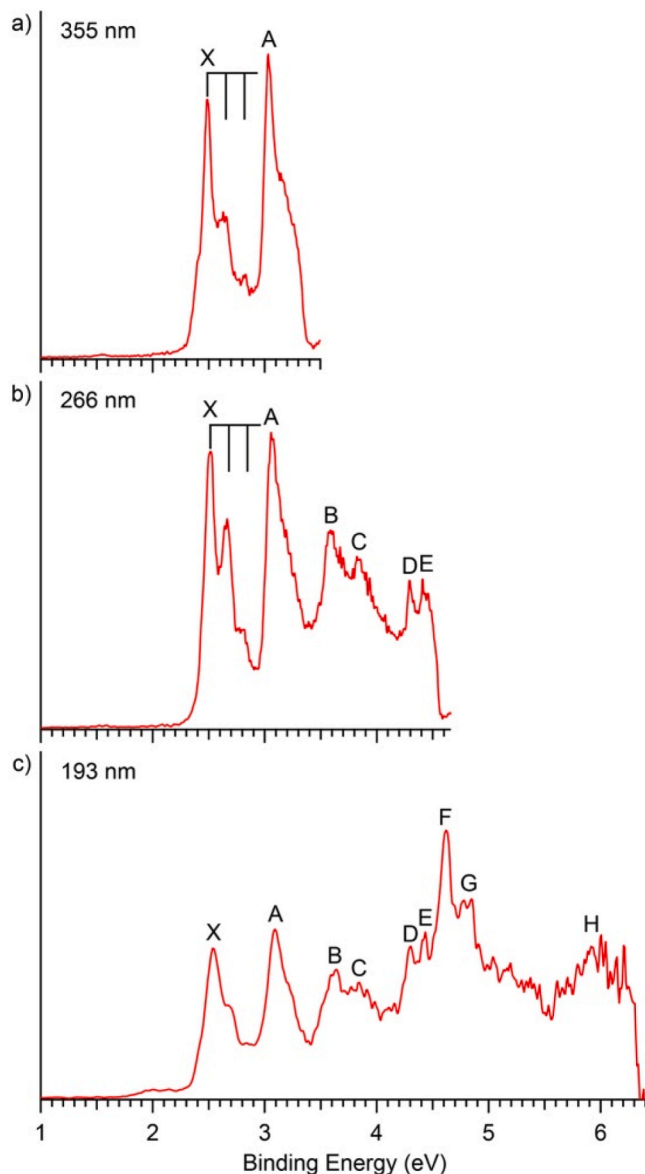


Fig. 2. The photoelectron spectra of Cu_2B_6^- at (a) 355 nm, (b) 266 nm, and (c) 193 nm.

Cu_2B_x clusters. The 193 nm spectra reveal more detachment transitions while the spectra taken at lower photon energies generally have better spectral resolution. The VDE of each detachment transition is measured from the band maximum, while the ADE is estimated by drawing a straight line at the leading edge of the detachment transition and then adding the instrumental resolution to the intercept with the binding energy axis. The ADE is usually only measured for the ground state transition (X), which also represents the electron affinity (EA) of the corresponding neutral Cu_2B_x cluster.

3.1.1. Cu_2B_5^-

The PES features of Cu_2B_5^- are relatively well resolved (Fig. 1). The 355 nm spectrum (Fig. 1a) displays one detachment band (X) centered at 2.32 eV, while its ADE is estimated to be 2.20 eV, i.e. the EA of Cu_2B_5 . At 266 nm (Fig. 1b), two broad bands (A and B) are observed with VDEs of 3.59 eV and 4.15 eV, respectively, following a large energy gap from band X. Band A appears to contain partially resolved vibrational structures. The 193 nm spectrum (Fig. 1c) reveals a well-resolved band C at 4.59 eV, followed by congested spectral features beyond 5 eV. A label (D) is given for the sake of discussion. The observed VDEs for all the PES

Table 2

The measured VDEs of Cu_2B_6^- compared with theoretical results of the GM structure at the PBE0/aug-cc-pVTZ level of theory. All energies are in eV.

	Final state and electron configuration	VDE ^a (exp)	VDE (theo)
X	$^1\text{A}_g \{ \dots (7a_g)^2(2a_u)^2(7b_u)^2(2b_g)^2(8b_u)^2(8a_g)^2(3a_u)^2(3b_g)^2(4a_u)^2(9a_g)^2(9b_u)^2(10a_g)^2(10b_u)^2(11a_g)^2(4b_g)^0 \}$	2.49	2.67
A	$^3\text{B}_g \{ \dots (7a_g)^2(2a_u)^2(7b_u)^2(2b_g)^2(8b_u)^2(8a_g)^2(3a_u)^2(3b_g)^2(4a_u)^2(9a_g)^2(9b_u)^2(10a_g)^2(10b_u)^2(11a_g)^1(4b_g)^1 \}$	3.03	2.93
	$^1\text{B}_g \{ \dots (7a_g)^2(2a_u)^2(7b_u)^2(2b_g)^2(8b_u)^2(8a_g)^2(3a_u)^2(3b_g)^2(4a_u)^2(9a_g)^2(9b_u)^2(10a_g)^2(10b_u)^2(11a_g)^1(4b_g)^1 \}$		3.16
B	$^3\text{A}_u \{ \dots (7a_g)^2(2a_u)^2(7b_u)^2(2b_g)^2(8b_u)^2(8a_g)^2(3a_u)^2(3b_g)^2(4a_u)^2(9a_g)^2(9b_u)^2(10a_g)^2(10b_u)^2(11a_g)^2(4b_g)^1 \}$	3.58	3.55
C	$^1\text{A}_u \{ \dots (7a_g)^2(2a_u)^2(7b_u)^2(2b_g)^2(8b_u)^2(8a_g)^2(3a_u)^2(3b_g)^2(4a_u)^2(9a_g)^2(9b_u)^2(10a_g)^2(10b_u)^2(11a_g)^2(4b_g)^1 \}$	3.84	3.94
D	$^3\text{B}_g \{ \dots (7a_g)^2(2a_u)^2(7b_u)^2(2b_g)^2(8b_u)^2(8a_g)^2(3a_u)^2(3b_g)^2(4a_u)^2(9a_g)^2(9b_u)^2(10a_g)^2(10b_u)^2(11a_g)^2(4b_g)^1 \}$	4.29	4.25
E	$^3\text{A}_u \{ \dots (7a_g)^2(2a_u)^2(7b_u)^2(2b_g)^2(8b_u)^2(8a_g)^2(3a_u)^2(3b_g)^2(4a_u)^2(9a_g)^2(9b_u)^2(10a_g)^2(10b_u)^2(11a_g)^2(4b_g)^1 \}$	4.41	4.41
	$^3\text{B}_g \{ \dots (7a_g)^2(2a_u)^2(7b_u)^2(2b_g)^2(8b_u)^2(8a_g)^2(3a_u)^2(3b_g)^2(4a_u)^2(9a_g)^2(9b_u)^2(10a_g)^2(10b_u)^2(11a_g)^2(4b_g)^1 \}$		4.43
F	$^3\text{B}_u \{ \dots (7a_g)^2(2a_u)^2(7b_u)^2(2b_g)^2(8b_u)^2(8a_g)^2(3a_u)^2(3b_g)^2(4a_u)^2(9a_g)^2(9b_u)^2(10a_g)^2(10b_u)^2(11a_g)^2(4b_g)^1 \}$	4.62	4.63
	$^1\text{B}_g \{ \dots (7a_g)^2(2a_u)^2(7b_u)^2(2b_g)^2(8b_u)^2(8a_g)^2(3a_u)^2(3b_g)^2(4a_u)^2(9a_g)^2(9b_u)^2(10a_g)^2(10b_u)^2(11a_g)^2(4b_g)^1 \}$		4.68
G	$^1\text{A}_u \{ \dots (7a_g)^2(2a_u)^2(7b_u)^2(2b_g)^2(8b_u)^2(8a_g)^2(3a_u)^2(3b_g)^2(4a_u)^2(9a_g)^2(9b_u)^2(10a_g)^2(10b_u)^2(11a_g)^2(4b_g)^1 \}$	4.79	4.77
	$^1\text{B}_g \{ \dots (7a_g)^2(2a_u)^2(7b_u)^2(2b_g)^2(8b_u)^2(8a_g)^2(3a_u)^2(3b_g)^2(4a_u)^2(9a_g)^2(9b_u)^2(10a_g)^2(10b_u)^2(11a_g)^2(4b_g)^1 \}$		4.78
	$^1\text{B}_u \{ \dots (7a_g)^2(2a_u)^2(7b_u)^2(2b_g)^2(8b_u)^2(8a_g)^2(3a_u)^2(3b_g)^2(4a_u)^2(9a_g)^2(9b_u)^2(10a_g)^2(10b_u)^2(11a_g)^2(4b_g)^1 \}$		5.17
H	$^3\text{B}_g \{ \dots (7a_g)^2(2a_u)^2(7b_u)^2(2b_g)^2(8b_u)^2(8a_g)^2(3a_u)^2(3b_g)^2(4a_u)^2(9a_g)^2(9b_u)^2(10a_g)^2(10b_u)^2(11a_g)^2(4b_g)^1 \}$	~5.9	5.48
	$^3\text{A}_u \{ \dots (7a_g)^2(2a_u)^2(7b_u)^2(2b_g)^2(8b_u)^2(8a_g)^2(3a_u)^2(3b_g)^2(4a_u)^2(9a_g)^2(9b_u)^2(10a_g)^2(10b_u)^2(11a_g)^2(4b_g)^1 \}$		5.48
	$^3\text{B}_u \{ \dots (7a_g)^2(2a_u)^2(7b_u)^2(2b_g)^2(8b_u)^2(8a_g)^2(3a_u)^2(3b_g)^2(4a_u)^2(9a_g)^2(9b_u)^2(10a_g)^2(10b_u)^2(11a_g)^2(4b_g)^1 \}$		5.48
	$^3\text{A}_g \{ \dots (7a_g)^2(2a_u)^2(7b_u)^2(2b_g)^2(8b_u)^2(8a_g)^2(3a_u)^2(3b_g)^2(4a_u)^2(9a_g)^2(9b_u)^2(10a_g)^2(10b_u)^2(11a_g)^2(4b_g)^1 \}$		5.48
	$^1\text{A}_g \{ \dots (7a_g)^2(2a_u)^2(7b_u)^2(2b_g)^2(8b_u)^2(8a_g)^2(3a_u)^2(3b_g)^2(4a_u)^2(9a_g)^2(9b_u)^2(10a_g)^2(10b_u)^2(11a_g)^2(4b_g)^1 \}$		5.57
	$^1\text{B}_g \{ \dots (7a_g)^2(2a_u)^2(7b_u)^2(2b_g)^2(8b_u)^2(8a_g)^2(3a_u)^2(3b_g)^2(4a_u)^2(9a_g)^2(9b_u)^2(10a_g)^2(10b_u)^2(11a_g)^2(4b_g)^1 \}$		5.57
	$^1\text{B}_u \{ \dots (7a_g)^2(2a_u)^2(7b_u)^2(2b_g)^2(8b_u)^2(8a_g)^2(3a_u)^2(3b_g)^2(4a_u)^2(9a_g)^2(9b_u)^2(10a_g)^2(10b_u)^2(11a_g)^2(4b_g)^1 \}$		5.58
	$^1\text{A}_u \{ \dots (7a_g)^2(2a_u)^2(7b_u)^2(2b_g)^2(8b_u)^2(8a_g)^2(3a_u)^2(3b_g)^2(4a_u)^2(9a_g)^2(9b_u)^2(10a_g)^2(10b_u)^2(11a_g)^2(4b_g)^1 \}$		5.58
	$^3\text{A}_g \{ \dots (7a_g)^2(2a_u)^2(7b_u)^2(2b_g)^2(8b_u)^2(8a_g)^2(3a_u)^2(3b_g)^2(4a_u)^2(9a_g)^2(9b_u)^2(10a_g)^2(10b_u)^2(11a_g)^2(4b_g)^1 \}$		5.63
	$^3\text{B}_u \{ \dots (7a_g)^2(2a_u)^2(7b_u)^2(2b_g)^2(8b_u)^2(8a_g)^2(3a_u)^2(3b_g)^2(4a_u)^2(9a_g)^2(9b_u)^2(10a_g)^2(10b_u)^2(11a_g)^2(4b_g)^1 \}$		5.71
	$^3\text{A}_u \{ \dots (7a_g)^2(2a_u)^2(7b_u)^2(2b_g)^2(8b_u)^2(8a_g)^2(3a_u)^2(3b_g)^2(4a_u)^2(9a_g)^2(9b_u)^2(10a_g)^2(10b_u)^2(11a_g)^2(4b_g)^1 \}$		5.82
	$^3\text{B}_g \{ \dots (7a_g)^2(2a_u)^2(7b_u)^2(2b_g)^2(8b_u)^2(8a_g)^2(3a_u)^2(3b_g)^2(4a_u)^2(9a_g)^2(9b_u)^2(10a_g)^2(10b_u)^2(11a_g)^2(4b_g)^1 \}$		5.91
	$^1\text{A}_u \{ \dots (7a_g)^2(2a_u)^2(7b_u)^2(2b_g)^2(8b_u)^2(8a_g)^2(3a_u)^2(3b_g)^2(4a_u)^2(9a_g)^2(9b_u)^2(10a_g)^2(10b_u)^2(11a_g)^2(4b_g)^1 \}$		5.93
	$^1\text{B}_g \{ \dots (7a_g)^2(2a_u)^2(7b_u)^2(2b_g)^2(8b_u)^2(8a_g)^2(3a_u)^2(3b_g)^2(4a_u)^2(9a_g)^2(9b_u)^2(10a_g)^2(10b_u)^2(11a_g)^2(4b_g)^1 \}$		6.03
	$^1\text{A}_g \{ \dots (7a_g)^2(2a_u)^2(7b_u)^2(2b_g)^2(8b_u)^2(8a_g)^2(3a_u)^2(3b_g)^2(4a_u)^2(9a_g)^2(9b_u)^2(10a_g)^2(10b_u)^2(11a_g)^2(4b_g)^1 \}$		6.20
	$^1\text{B}_u \{ \dots (7a_g)^2(2a_u)^2(7b_u)^2(2b_g)^2(8b_u)^2(8a_g)^2(3a_u)^2(3b_g)^2(4a_u)^2(9a_g)^2(9b_u)^2(10a_g)^2(10b_u)^2(11a_g)^2(4b_g)^1 \}$		6.33

^a The uncertainty of the VDEs was ± 0.02 eV.

bands are summarized in Table 1, where they are compared with theoretical results (*vide infra*).

3.1.2. Cu_2B_6^-

The photoelectron spectra of Cu_2B_6^- (Fig. 2) are more complicated due to its open shell nature, but still well resolved. Two PES bands (X and A) are observed at 355 nm (Fig. 2a). A short vibrational progression is resolved for band X with an average spacing of 1330 (50) cm^{-1} ; its VDE is measured to be 2.49 eV and its ADE or the EA of neutral Cu_2B_6 is estimated.

To be 2.30 eV. Band A is centered at 3.03 eV with a relatively broad width due to excitation of low frequency vibrations. In the 266 nm spectrum (Fig. 2b), the vibrational progression of band X is again well resolved. In addition, two closely-spaced bands B and C are observed at 3.58 eV and 3.84 eV, respectively. Two more closely-spaced bands D and E are observed near the detachment threshold at 4.29 eV and 4.41 eV, respectively. The 193 nm spectrum (Fig. 2c) shows that the spectral features become congested beyond 4 eV. Two intense bands F and G are observed at 4.62 eV and 4.79 eV, respectively. The broad features in the high binding energy side are tentatively labeled as H. All the observed features and their VDEs are given in Table 2 and compared with theoretical results.

3.1.3. Cu_2B_7^-

The photoelectron spectra of Cu_2B_7^- (Fig. 3) are also congested, but the spectral features are relatively sharp and well resolved, indicating that its structure is stable and rigid with minor geometry changes upon electron detachment. In the 355 nm spectrum (Fig. 3a), the ground state band X at 3.09 eV is observed to contain vibrational features of two modes with spacings of 690 (30) cm^{-1} and 1370 (40) cm^{-1} . The ADE of band X or the EA of Cu_2B_7 is measured to be 3.03 eV. In the 266 nm spectrum (Fig. 3b), the vibrational progression of the high frequency mode of band X is fully observed. In addition, three more PES bands (A, B, C) are observed. Band A at 3.63 eV also contains a short vibrational progression with a spacing of 1370 (70) cm^{-1} , the same as the high frequency mode of band X. The weaker band B at 3.96 eV is broad, due to

unresolved low-frequency vibrational features. A sharp and intense band C appears to be cut off at 266 nm. In the 193 nm spectrum (Fig. 3c), the VDE of band C is observed to be 4.47 eV. Two more sharp bands D and E are resolved at 4.80 eV and 5.01 eV, respectively, in the 193 nm spectrum. Beyond 5 eV, the spectral features become broader and less well resolved. Two broad bands at around 5.4 eV (F) and 6.1 eV (G) are tentatively labeled. The weak features at the low binding energy side (X'' , X' , $*$) are due to the existence of isomers or contamination. The VDEs of all the observed features are given in Table 3 in comparison with theoretical results.

3.2. Theoretical results

The GM structures and low-lying isomers of Cu_2B_x^- ($x = 5-7$) are presented in Fig. 4. More low-lying structures are shown in Appendix A (Figs. S1-S3). Comparison between the first experimental VDE and ADE with those of the corresponding GM structures is given in Table 4, where the VDE₁ for the first two low-lying isomers of Cu_2B_7^- are also given.

3.2.1. Cu_2B_5^-

The GM structure of Cu_2B_5^- is significantly lower in energy than all other low-lying isomers at both the PBE0 and CCSD(T) levels of theory (Fig. 4a). It has a closed-shell quasi-planar structure (C_{2v} , ^1A), consisting of a B_5 motif with the two Cu atoms bonded to the two apex B atoms. The trapezoidal or double-chain structure of the B_5 motif is similar to the GM of the bare B_5 cluster, which was the very first boron cluster to be characterized by joint PES and theoretical studies [78]. The HOMO-LUMO gap was computed to be 2.24 eV at the PBE0 level of theory, indicating that the GM of Cu_2B_5^- is a highly stable electronic system. Iso1 to Iso4 all involve two Cu atoms bonded to the trapezoidal B_5 motif in different fashions. In Iso1, Iso3, and Iso4, there is Cu-Cu bonding, whereas Iso2 is very similar to the GM except one of the Cu atom bridging two B atoms. All these isomers are at least 7.0 kcal/mol higher in energy than the GM at both PBE0 and CCSD(T) levels of theory.

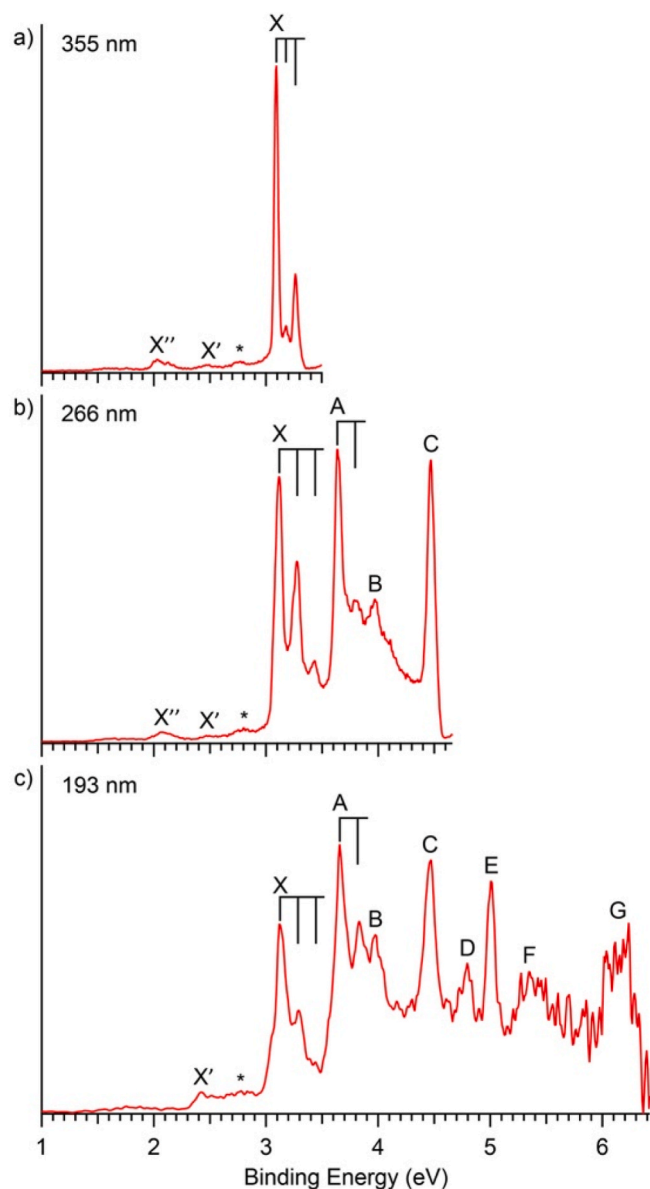


Fig. 3. The photoelectron spectra of Cu_2B_7^- at (a) 355 nm, (b) 266 nm, and (c) 193 nm.

3.2.2. Cu_2B_6^-

The GM of Cu_2B_6^- (C_{2h} , 2B_g) consists of two Cu atoms forming two single Cu–B bonds via the vertices of a double-chain B_6 motif (Fig. 4b), similar to the GM of Au_2B_6^- [56]. The HOMO–SOMO (beta MOs) gap was computed to be 1.44 eV, and the SOMO–LUMO gap (alpha MOs) was computed to be 2.9 eV, suggesting that Cu_2B_6^- or the closed-shell $\text{Cu}_2\text{B}_6^{2-}$ are highly stable electronic systems. The double-chain B_6 motif in Cu_2B_6^- is slightly different from the GM of the bare B_6^- cluster, which has a similar planar structure, but with higher symmetry (D_{2h}) [79]. The first low-lying isomer Iso1 (C_s , $^2A''$) is quite close in energy to the GM, 1.7 kcal/mol at the CCSD(T) level and 4.3 kcal/mol at the PBE0 level. The B_6 motif in Iso1 forms a partial hexagon with one of the Cu atoms completing the hexagonal structure and the other Cu atom bridging the Cu–B bond on the asymmetric hexagon. Iso3 (C_{2v}) and Iso4 (C_1) are built on a similar partial hexagonal B_6 motif with the two Cu atoms bonded in different fashions. Iso2 (2A , C_1) consists of the same double-chain B_6 motif as the GM, except that the two Cu atoms are on one side. All these isomers are significantly higher in energy than the GM structure.

3.2.3. Cu_2B_7^-

The GM structure of Cu_2B_7^- at the PBE0 level consists of a double-chain B_7 motif with the two Cu atoms bonded to the two apex B atoms (Fig. 4c), similar to that in the GM of Cu_2B_5^- . The GM of the bare B_7^- cluster in fact has a hexagonal structure with a triplet spin state (C_{6v} , 3A_1), whereas the double-chain structure is a higher energy isomer, but was observed experimentally [39]. The double-chain GM of Cu_2B_7^- is identical to that of Au_2B_7^- [55]. Its large calculated HOMO–LUMO gap of 2.54 eV suggests that it is a highly stable electronic system. However, Iso1 (D_{7h} , 3A_1) and Iso2 (C_{2v} , 1A_1) are lower in energy than the double-chain GM at the CCSD(T) level (Fig. 4c). Both Iso1 and Iso2 have similar inverse sandwich structures with different spin states, consisting of a heptagonal B_7 ring capped by the two Cu atoms. These are interesting structures that have been observed only for di-lanthanide hepta-boron clusters (Ln_2B_7^-) [54], but not for transition-metal- B_7 clusters. The only inverse sandwich clusters involving a transition metal was Ta_2B_6^- (D_{6h} , $^2A_{1g}$) [61]. We will show below that the true GM structure observed experimentally for Cu_2B_7^- is indeed the double-chain structure. In fact, the PES features, as well as the resolved vibrational structures of Cu_2B_7^- (Fig. 3) are similar to those observed for Au_2B_7^- [50]. Iso3 (C_s , $^1A'$) is composed of a hexagonal B_7 and a Cu_2 unit atop the B_7 plane, whereas Iso4 (2A , C_1) consists of a double-chain B_7 motif with a Cu_2 unit on one side of the double-chain. Both isomers are significantly higher in energy than the GM structure at both levels of theory.

In order to compute the ADEs of the GM structures of Cu_2B_x^- ($x = 5–7$), we also optimized the corresponding neutral structures without any extensive GM searches. The calculated ADEs for the GM of each

Table 3

The measured VDEs of Cu_2B_7^- compared with theoretical results of the GM structure at the PBE0/aug-cc-pVTZ level of theory. All energies are in eV.

Final state and electron configuration	VDE ^a (exp)	VDE (theo)
X $^2A_2 \{ \dots (2b_1)^2(7b_2)^2(8a_1)^2(2a_2)^2(3b_1)^2(3a_2)^2(8b_2)^2(9a_1)^2(4b_1)^2(10a_1)^2(9b_2)^2(10b_2)^2(11a_1)^2(12a_1)^2(4a_2)^1 \}$	3.09	3.08
A $^2A_1 \{ \dots (2b_1)^2(7b_2)^2(8a_1)^2(2a_2)^2(3b_1)^2(3a_2)^2(8b_2)^2(9a_1)^2(4b_1)^2(10a_1)^2(9b_2)^2(10b_2)^2(11a_1)^2(12a_1)^1(4a_2)^2 \}$	3.63	3.59
B $^2A_1 \{ \dots (2b_1)^2(7b_2)^2(8a_1)^2(2a_2)^2(3b_1)^2(3a_2)^2(8b_2)^2(9a_1)^2(4b_1)^2(10a_1)^2(9b_2)^2(10b_2)^2(11a_1)^1(12a_1)^2(4a_2)^2 \}$	3.96	3.96
C $^2B_2 \{ \dots (2b_1)^2(7b_2)^2(8a_1)^2(2a_2)^2(3b_1)^2(3a_2)^2(8b_2)^2(9a_1)^2(4b_1)^2(10a_1)^2(9b_2)^2(10b_2)^1(11a_1)^2(12a_1)^2(4a_2)^2 \}$	4.47	4.26
D $^2B_2 \{ \dots (2b_1)^2(7b_2)^2(8a_1)^2(2a_2)^2(3b_1)^2(3a_2)^2(8b_2)^2(9a_1)^2(4b_1)^2(10a_1)^2(9b_2)^1(10b_2)^2(11a_1)^2(12a_1)^2(4a_2)^2 \}$	4.80	4.74
E $^2A_1 \{ \dots (2b_1)^2(7b_2)^2(8a_1)^2(2a_2)^2(3b_1)^2(3a_2)^2(8b_2)^2(9a_1)^2(4b_1)^2(10a_1)^1(9b_2)^2(10b_2)^2(11a_1)^2(12a_1)^2(4a_2)^2 \}$	5.01	4.79
F $^2B_1 \{ \dots (2b_1)^2(7b_2)^2(8a_1)^2(2a_2)^2(3b_1)^2(3a_2)^2(8b_2)^2(9a_1)^2(4b_1)^1(10a_1)^2(9b_2)^2(10b_2)^2(11a_1)^2(12a_1)^2(4a_2)^2 \}$	~5.4	5.36
$^2B_2 \{ \dots (2b_1)^2(7b_2)^2(8a_1)^2(2a_2)^2(3b_1)^2(3a_2)^2(8b_2)^1(9a_1)^2(4b_1)^2(10a_1)^2(9b_2)^2(10b_2)^2(11a_1)^2(12a_1)^2(4a_2)^2 \}$		5.63
$^2A_1 \{ \dots (2b_1)^2(7b_2)^2(8a_1)^2(2a_2)^2(3b_1)^2(3a_2)^2(8b_2)^2(9a_1)^1(4b_1)^2(10a_1)^2(9b_2)^2(10b_2)^2(11a_1)^2(12a_1)^2(4a_2)^2 \}$		5.63
$^2A_2 \{ \dots (2b_1)^2(7b_2)^2(8a_1)^2(2a_2)^2(3b_1)^2(3a_2)^1(8b_2)^2(9a_1)^2(4b_1)^2(10a_1)^2(9b_2)^2(10b_2)^2(11a_1)^2(12a_1)^2(4a_2)^2 \}$		5.63
$^2B_1 \{ \dots (2b_1)^2(7b_2)^2(8a_1)^2(2a_2)^2(3b_1)^1(3a_2)^2(8b_2)^2(9a_1)^2(4b_1)^2(10a_1)^2(9b_2)^2(10b_2)^2(11a_1)^2(12a_1)^2(4a_2)^2 \}$		5.64
G $^2A_2 \{ \dots (2b_1)^2(7b_2)^2(8a_1)^2(2a_2)^1(3b_1)^2(3a_2)^2(8b_2)^2(9a_1)^2(4b_1)^2(10a_1)^2(9b_2)^2(10b_2)^2(11a_1)^2(12a_1)^2(4a_2)^2 \}$	~6.1	5.93
$^2A_1 \{ \dots (2b_1)^2(7b_2)^2(8a_1)^1(2a_2)^2(3b_1)^2(3a_2)^2(8b_2)^2(9a_1)^2(4b_1)^2(10a_1)^2(9b_2)^2(10b_2)^2(11a_1)^2(12a_1)^2(4a_2)^2 \}$		6.01
$^2B_1 \{ \dots (2b_1)^1(7b_2)^2(8a_1)^2(2a_2)^2(3b_1)^2(3a_2)^2(8b_2)^2(9a_1)^2(4b_1)^2(10a_1)^2(9b_2)^2(10b_2)^2(11a_1)^2(12a_1)^2(4a_2)^2 \}$		6.02
$^2B_2 \{ \dots (2b_1)^2(7b_2)^1(8a_1)^2(2a_2)^2(3b_1)^2(3a_2)^2(8b_2)^2(9a_1)^2(4b_1)^2(10a_1)^2(9b_2)^2(10b_2)^2(11a_1)^2(12a_1)^2(4a_2)^2 \}$		6.08

^a The uncertainty of the VDEs was ± 0.02 eV.

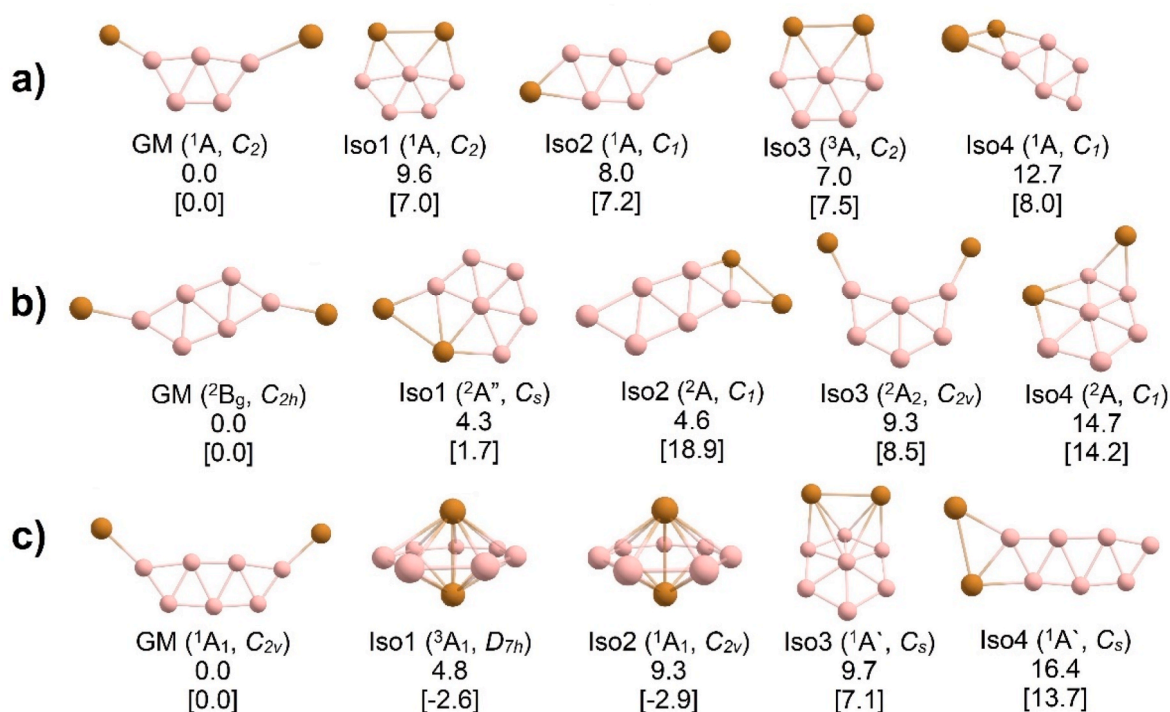


Fig. 4. The GM structures and low-lying isomers of (a) Cu_2B_5^- , (b) Cu_2B_6^- , and (c) Cu_2B_7^- . Relative energies are given in kcal/mol at the PBE0/aug-cc-pVTZ + ZPE level and the CCSD(T)/def2-TZVP level [in brackets].

Table 4

Comparison of the experimental ADE and VDE_1 with the calculated values at the PBE0/aug-cc-pVTZ and CCSD(T)/aug-cc-pVTZ levels of theory for the GM of Cu_2B_x^- ($x = 5-7$) and two low-lying isomers of Cu_2B_7^- . All energies are in eV.

	Final state	VDE_1/ADE (theo)		VDE_1/ADE (exp) ^a
		PBE0	CCSD(T)	
Cu_2B_5^- (GM, C_2 , 1A)	2A	2.15/	2.22/	2.32/2.20
		2.07	2.12	
Cu_2B_6^- (GM, C_{2h} , 2B_g)	1A_g	2.67/	2.51/	2.49/2.30
		2.56	2.37	
Cu_2B_7^- (GM, C_{2v} , 1A_1)	2A_2	3.08/	3.16/	3.09/3.03
		2.97	3.02	
Cu_2B_7^- (Iso1, D_{7h} , 3A_1)	2E_1	2.46/-	2.49/-	2.48 (X')/-
Cu_2B_7^- (Iso2, C_{2v} , 1A_1)	2A_1	2.19/-	2.46/-	2.03 (X')/-

^a The experimental uncertainty was ± 0.02 eV.

species are given in Tables 4 and in comparison with the experimental data.

4. Discussion

4.1. Comparison between experiment and theory and confirmation of the GM structures of Cu_2B_x^-

The experimental PES data have been critical to verify the GM structures of size-selected clusters, in particular, for boron and metal-boride clusters [9,10]. The calculated VDEs for the GM structures are compared with the experimental PES results in Table 1–3 for Cu_2B_x^- ($x = 5-7$), respectively, and presented as vertical bars in Fig. 5 on the 193 nm spectra. Since the GM structures of Cu_2B_5^- and Cu_2B_7^- are closed-shell, each occupied valence MO results in one detachment channel, leading to a doublet final state (Tables 1 and 3). The open-shell GM of Cu_2B_6^- can lead to both singlet and triplet final states, resulting in more congested spectral features (Table 2).

4.1.1. Cu_2B_5^-

The calculated ADE/ VDE_1 for the GM of Cu_2B_5^- (2.22/2.12 eV) at the CCSD(T) level are in good agreement with the experimental values of 2.32/2.20 eV (Table 4). Even though the PBE0 level seems to underestimate the VDEs in comparison with the experimental data, the pattern of the computed VDEs at the PBE0 level for the GM of Cu_2B_5^- is consistent with the observed PES bands, as shown in Table 1 and Fig. 5a. Band X is derived from electron detachment from the HOMO (14a), which involves weak σ -bonding in the B_5 motif (Fig. S4), consistent with the relatively sharp PES band. The VDE of 2.15 eV computed at the PBE0 level is lower than the experimental value (2.32 eV) by 0.17 eV. The next detachment channel from the HOMO-1 (13b) gives a computed VDE of 3.60 eV, compared well with the experimental VDE of 3.59 eV for band A. The HOMO-1 (13b) is an in-plane σ MO, involving strong peripheral B–B bonding (Fig. S4), consistent with the broad band A. According to Table 1, band B contains two very close VDEs and VDEs computed to be 4.13 and 4.21 eV from the HOMO-2 (13a) and HOMO-3 (12b), respectively. The 13a orbital involves peripheral B–B σ -bonding on the B_5 motif, while 12b is a Cu–B bonding MO. The PES band C at 4.59 eV is mainly from detachment from the HOMO-4 (11b) with a computed VDE of 4.56 eV. The 11b MO is a π -orbital on the B_5 motif (Fig. S4). The detachment from the HOMO-5 (12a) with a computed VDE of 4.70 eV may also contribute to band C. The 12a MO contains contributions from both the B_5 motif and the Cu 3d orbitals (Fig. S4). HOMO-6 (11a) and HOMO-7 (10b) give similar computed VDEs of 5.3 eV. These two orbitals and the next six MOs are due to the 3d lone pairs of the Cu atoms, which are expected to yield closely-spaced detachment channels, consistent with the broad PES features beyond 5 eV (Fig. 1). Overall, the computed VDEs are in good agreement with the experimental spectral pattern (Fig. 5a), confirming the planar C_2 (1A) structure as the GM of Cu_2B_5^- .

4.1.2. Cu_2B_6^-

The calculated ADE/ VDE_1 for the GM structure of Cu_2B_6^- are 2.51/2.37 eV at the CCSD(T) level of theory (Table 4), consistent with the experimental data of 2.49/2.30 eV. The corresponding values of 2.67/2.56 eV at the PBE0 level are overestimated in comparison with the

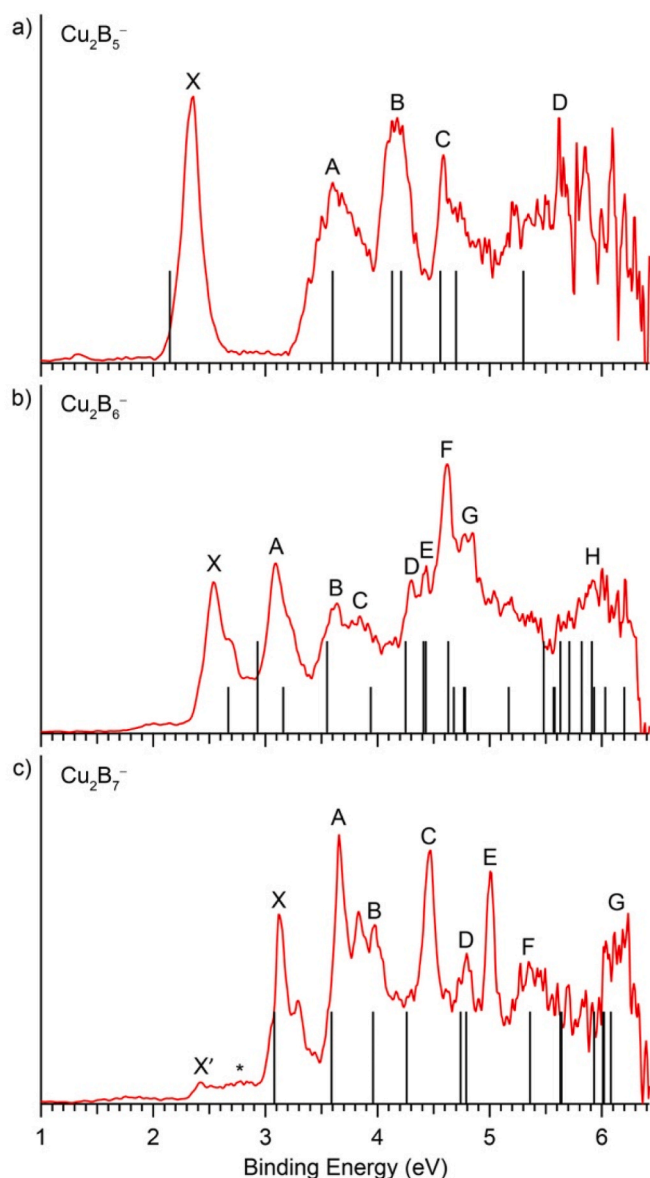


Fig. 5. Comparison between the 193 nm photoelectron spectra and the theoretical results for (a) Cu_2B_5^- , (b) Cu_2B_6^- , (c) Cu_2B_7^- . The vertical bars indicate computed VDEs for the GM structure in each case at the PBE0/aug-cc-pVTZ level of theory. For Cu_2B_6^- , the shorter and longer bars correspond to transitions to singlet and triplet final states, respectively.

experimental data. The first VDE comes from detachment from the SOMO ($4b_g$), which is a π bonding orbital of the B_6 motif (Fig. S5). The observed vibrational progression for band X (Fig. 2) should correspond to the symmetric B–B breathing vibrational mode of the B_6 motif with a computed frequency of 1360 cm^{-1} , agreeing well with the observed frequency of $1330(50)\text{ cm}^{-1}$. The vibrational progression and frequency for band X of Cu_2B_6^- are very similar to those observed in the photoelectron spectra of Au_2B_6^- [56], which displayed a vibrational progression with a measured frequency of $1350(30)\text{ cm}^{-1}$. The next detachment from the HOMO ($11a_g$) results in two final states, a high spin (3B_g) and low spin (1B_g) states with the computed VDE₂ (2.93 eV) and VDE₃ (3.16 eV) at the PBE0 level of theory, which are in good agreement with the observed band A. The detachment from the HOMO-1 ($10b_u$) also results in a triple and singlet final states with computed VDE₄ and VDE₅ of 3.55 eV and 3.94 eV, agreeing well with the observed band B (3.58 eV) and band C (3.84 eV), respectively (Table 2 and Fig. 5). Both the HOMO ($11a_g$) and HOMO-1 ($10b_u$) are mainly σ -bonding orbitals of

the B_6 motif (Fig. S5). Detachment from the next four filled MOs [HOMO-2 ($10a_g$), HOMO-3 ($9b_u$), HOMO-4 ($9a_g$), and HOMO-5 ($4a_u$)], which are all B_6 -based orbitals, give rise to a set of closely-spaced detachment channels, accounting for the congested spectral features from bands D to G (Table 2 and Fig. 5b). Following an energy gap, another set of closely-spaced detachment channels (VDE: 5.48–6.33 eV), all from the Cu 3d lone pairs (Fig. S5), is in accord with the congested spectral features in the high binding energy side of the 193 nm spectrum of Cu_2B_6^- (Table 2 and Fig. 5b). The good agreement between the computed VDEs and the experimental spectral pattern provides considerable credence for the C_{2h} (2B_g) GM structure of Cu_2B_6^- .

4.1.3. Cu_2B_7^-

The potential energy surface of Cu_2B_7^- seems to be more complicated than that of Au_2B_7^- , for which the double-chain C_{2v} structure is the overwhelming global minimum [55]. The double-chain C_{2v} structure is the GM for Cu_2B_7^- at the PBE0 level, but at the CCSD(T) level the inverse sandwich Iso2 (C_{2v} , 1A_1) is the global minimum with its triplet counterpart Iso1 (D_{7h} , 3A_1) only 0.3 kcal/mol higher in energy (Fig. 4). However, the experimental PES data suggest that the double-chain C_{2v} structure is the true GM for Cu_2B_7^- . First of all, the computed VDE₁/ADE of the C_{2v} Cu_2B_7^- at both the PBE0 level (3.08/2.97 eV) and the CCSD(T) level (3.16/3.02 eV) are in excellent agreement with the experimental values of 3.09/3.03 eV (Table 4). On the other hand, the computed VDE₁ values of Iso1 (2.46 eV) and Iso2 (2.19 eV) at the PBE0 level are in good agreement with the weak features X' (2.48 eV) and X'' (2.03 eV), which are present as minor isomers. Second, the vibrational progression and frequencies resolved for the X band of Cu_2B_7^- are very similar to those observed for Au_2B_7^- [55]. The two frequencies observed for Au_2B_7^- were $1380(40)\text{ cm}^{-1}$ due to the totally symmetric B–B vibration of the double-chain B_7 motif and $790(40)\text{ cm}^{-1}$ due to the Au–B symmetric stretching mode. The corresponding frequencies observed for Cu_2B_7^- are $1370(40)\text{ cm}^{-1}$ and $690(30)\text{ cm}^{-1}$, in comparison with the computed B–B stretching frequency of 1342 cm^{-1} and the Cu–B stretching frequency of 660 cm^{-1} . The larger Au–B stretching frequency is consistent with the strong Au–B covalent bond due to the strong relativistic effects of Au [80]. Therefore, there is strong evidence that the true GM of Cu_2B_7^- is indeed the C_{2v} double-chain structure, indicating that the PBE0 method is more reliable for Cu_2B_7^- .

The first PES band (X) is due to detachment of an electron from the HOMO ($4a_2$) of the C_{2v} GM of Cu_2B_7^- , which is a π bonding orbital of the double-chain B_7 motif with a weak antibonding interaction with the two Cu atoms (Fig. S6). Thus, removal of a HOMO electron is expected to weaken the π -bonding of the B_7 motif and slightly strengthen the Cu–B bonds, in accord with the observed vibrational progressions, as discussed above. Electron detachment from the HOMO-1 ($12a_1$) results in VDE₂ of 3.59 eV, which is in good agreement with the measured VDE of band A of 3.63 eV (Table 3). Electron detachment from the HOMO-2 ($11a_1$) gives a computed VDE₃ of 3.96 eV, in excellent agreement with the experimental band B of 3.96 eV. The experimental PES bands C/D/E/F with VDEs of 4.47/4.80/5.01/5.4 eV are also in good agreement with the corresponding theoretical VDEs of 4.26/4.74/4.79/5.36 eV from detachment from HOMO-3($10b_2$)/HOMO-4($9b_2$)/HOMO-5($10a_1$)/HOMO-6($4b_1$), respectively. All these valence MOs involve the B_7 motif with minor contributions from the Cu atoms (Fig. S6). Starting from HOMO-7 ($9a_1$) are Cu 3d-based lone pairs, which give a set of closely-spaced detachment channels in accord with the congested spectral features in the high binding energy side (Table 3 and Fig. 5c). Thus, the good agreement between the computed VDEs and the experimental spectral pattern provides further confirmation about the C_{2v} GM for Cu_2B_7^- .

4.2. Chemical bonding in the GM structures of Cu_2B_x^- ($x = 5-7$)

We used AdNDP analyses to decipher the overall bonding properties from the canonical MOs. The AdNDP bonding patterns of the GM

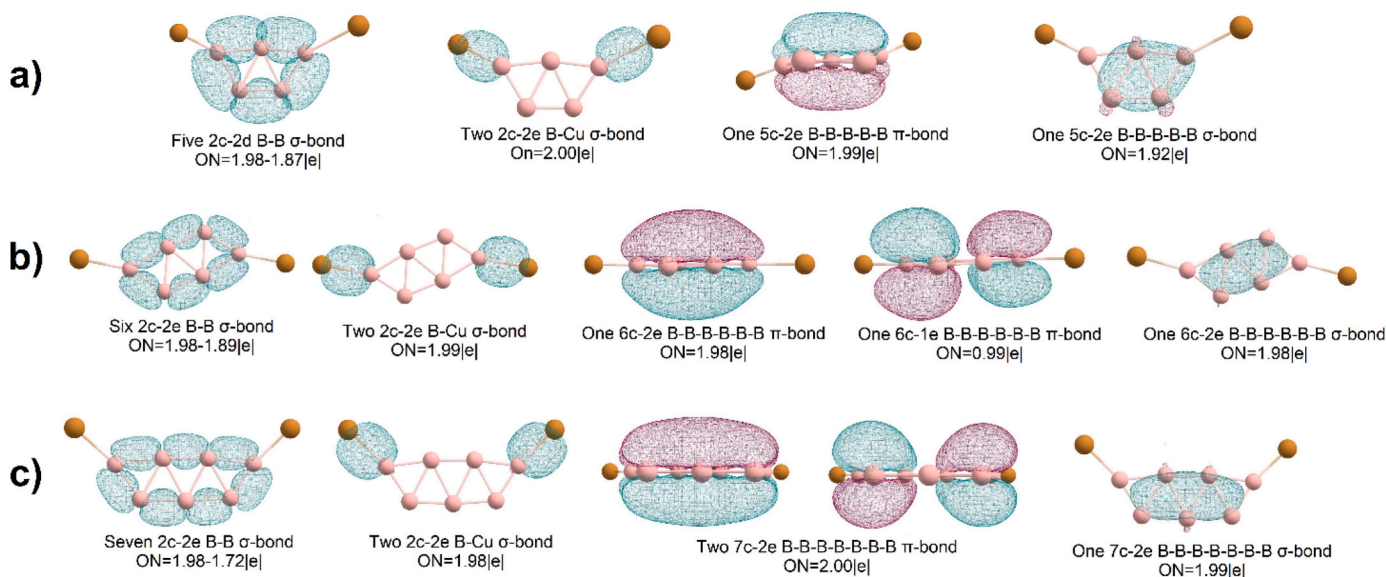


Fig. 6. AdNDP bonding analyses for the GM structures of Cu_2B_x^- . a) Cu_2B_5^- , b) Cu_2B_6^- , c) Cu_2B_7^- .

structures of Cu_2B_x^- ($x = 5-7$) are presented in Fig. 6. In all cases we omitted the ten localized 1c-2e 3d lone pairs on the Cu atoms. The occupation numbers (ONs) of all the 3d lone pairs are within 1.95–2.00 |e|, consistent with their nonbonding nature. The bonding patterns in the three clusters exhibit some similarities. They all contain x strong 2c-2e σ bonds on the periphery of the double-chain B_x motif, two terminal 2c-2e Cu–B σ bonds, one delocalized x -2e σ bond, and different delocalized π bonds. The Cu_2B_5^- cluster contains one delocalized 5c-2e π bond, which together with the delocalized σ bond renders it doubly aromatic, because each delocalized system fulfills the $4N + 2$ electron counting rule for aromaticity. The Cu_2B_6^- and Cu_2B_7^- clusters each contain two delocalized π bonds, which make them π antiaromatic, but σ aromatic due to the two delocalized σ electrons. The π aromaticity is consistent with their elongated shapes. In the case of Cu_2B_6^- , there are only three π electrons, but it is expected to be similar to the 4π electron closed-shell $\text{Cu}_2\text{B}_6^{2-}$ species.

The structure and bonding in the Cu_2B_x^- ($x = 5-7$) series are similar to those in the corresponding Au_2B_x^- , B_xH_2^- , and $\text{B}_x(\text{BO})_2^-$ systems [55,56,81,82], which contain strong terminal B–Au, B–H, and B–BO covalent bonds, respectively. This similarity is somewhat surprising because Cu is not known to form covalent bonds due to its low electronegativity. Apparently, the high stabilities of the double-chain B_x motifs dictate the structures and bonding in these smaller Cu_2B_x^- clusters. We note that the Cu_2B_8^- cluster is a charge-transfer complex between the B_8^{2-} borozene and a Cu_2^+ unit [65], due to the high stability of the borozene [50] and the low electronegativity of Cu. On the other hand, B_8H_2^- and $\text{B}_8(\text{BO})_2^-$ both have the double-chain structures with strong terminal B–H and B–BO covalent bonds [81,82]. We expect that Au_2B_8^- should have a similar double-chain structure due to the strong B–Au covalent bonding [80].

5. Conclusions

We report a combined photoelectron spectroscopy and computational study of a series of di-copper boron clusters, Cu_2B_x^- ($x = 5-7$). Well-resolved photoelectron spectra are obtained and used to elucidate their structures and chemical bonding. All three clusters are found to possess structures consisting of an elongated double-chain boron motif with the copper atoms covalently bonded to terminal boron atoms at the two apex sites. The closed-shell Cu_2B_5^- is found to be particularly stable due to the double aromaticity of the B_5 motif, whereas for Cu_2B_7^- there is experimental and theoretical evidence for the existence of unexpected

inverse-sandwich-type low-lying isomers. The covalent Cu–B bonds found in the Cu_2B_x^- ($x = 5-7$) clusters are surprising, which is due to the high stability of the double-chain B_x motif in this size range, whereas the ionic bonding nature of Cu is manifested in the Cu_2B_8^- cluster. The current work provides further insight into the interaction between copper and boron and the size-dependence of Cu–B bonding from covalent to ionic with increasing cluster size.

Author statement

Anton S. Pozdeev: Calculation, Structure and bonding analyses, Writing - original draft. Maksim Kulichenko: Calculation, Structure and bonding analyses. Wei-Jia Chen: Data curation and analyses, Writing - original draft. Hyun Wook Choi: Data Curation, Investigation. Alexander I. Boldyrev: Supervision of theoretical calculations, Conceptualization, Reviewing and Editing preparation. Lai-Sheng Wang: Supervision and Conceptualization of experiment and project, Investigation, Reviewing and Editing preparation.

Declaration of competing interest

The authors declare that they have no known competing financial interests or personal relationships that could have appeared to influence the work reported in this paper.

Data availability

Data will be made available on request.

Acknowledgments

The experiment done at Brown University was supported by the National Science Foundation (CHE-2053541). Computational resources were supported by the Center for High Performance Computing at the University of Utah.

Appendix A. Supplementary data

Supplementary data to this article can be found online at <https://doi.org/10.1016/j.solidstatesciences.2023.107248>.

References

- [1] B. Albert, H. Hillebrecht, Boron: elementary challenge for experimenters and theoreticians, *Angew. Chem., Int. Ed.* 48 (2009) 8640–8668.
- [2] E.D. Jemmis, D.L.V.K. Prasad, Icosahedral B12, macropolyhedral boranes, rhombohedral boron and boron-rich solids, *J. Solid State Chem.* 179 (2006) 2768–2774.
- [3] A.R. Oganov, J. Chen, C. Gatti, Y. Ma, Y. Ma, C.W. Glass, Z. Liu, T. Yu, O. O. Kurakevych, V.L. Solozhenko, Ionic high-pressure form of elemental boron, *Nature* 457 (2009) 863–867.
- [4] H. Tang, S. Ismail-Beigi, Novel precursors for boron nanotubes: the competition of two-center and three-center bonding in boron sheets, *Phys. Rev. Lett.* 99 (2007), 115501.
- [5] X. Yang, Y. Ding, J. Ni, Ab initio prediction of stable boron sheets and boron nanotubes: structure, stability, and electronic properties, *Phys. Rev. B* 77 (2008), 041402.
- [6] A.N. Alexandrova, A.I. Boldyrev, H.J. Zhai, L.S. Wang, All-boron aromatic clusters as potential new inorganic ligands and building blocks in chemistry, *Coord. Chem. Rev.* 250 (2006) 2811–2866.
- [7] E. Oger, N.R. Crawford, R. Kelting, P. Weis, M.M. Kappes, R. Ahlrichs, Boron cluster cations: transition from planar to cylindrical structures, *Angew. Chem. Int. Ed.* 46 (2007) 8503–8506.
- [8] A.P. Sergeeva, I.A. Popov, Z.A. Piazza, W.L. Li, C. Romanescu, L.S. Wang, A. I. Boldyrev, Understanding boron through size-selected clusters: structure, chemical bonding, and fluxionality, *Acc. Chem. Res.* 47 (2014) 1349–1358.
- [9] L.S. Wang, Photoelectron spectroscopy of size-selected boron clusters: from planar structures to borophenes and borospherenes, *Int. Rev. Phys. Chem.* 35 (2016) 69–142.
- [10] T. Jian, X. Chen, S.D. Li, A.I. Boldyrev, J. Li, L.S. Wang, Probing the structures and bonding of size-selected boron and doped-boron clusters, *Chem. Soc. Rev.* 48 (2019) 3550–3591.
- [11] S. Pan, J. Barroso, S. Jalife, T. Heine, K.R. Asmics, G. Merino, Fluxional boron clusters: from theory to reality, *Acc. Chem. Res.* 52 (2019) 2732–2744.
- [12] A. Ricca, C.W. Bauschlicher, The structure and stability of Bn⁺ clusters, *Chem. Phys. Lett.* 208 (1996) 233–242.
- [13] I. Boustani, Systematic ab initio investigation of bare boron clusters: determination of the geometry and electronic structures of Bn (n = 2–14), *Phys. Rev. B* 55 (1997) 16426–16438.
- [14] J.E. Fowler, J.M. Ugalde, The curiously stable B13⁺ cluster and its neutral and anionic counterparts: the advantages of planarity, *J. Phys. Chem.* 104 (2000) 397–403.
- [15] T.B. Tai, N.M. Tam, M.T. Nguyen, Structure of boron clusters revisited, Bn with n = 14–20, *Chem. Phys. Lett.* 530 (2012) 71–76.
- [16] S.G. Xu, Y.J. Zhao, J.H. Liao, X.B. Yang, Understanding the stable boron clusters: a bond model and first-principles calculations based on high-throughput screening, *J. Chem. Phys.* 142 (2015), 214307.
- [17] H.J. Zhai, A.N. Alexandrova, K.A. Birch, A.I. Boldyrev, L.S. Wang, Hepta- and octa-coordinated boron in molecular wheels of 8- and 9-atom boron clusters: observation and confirmation, *Angew. Chem. Int. Ed.* 42 (2003) 6004–6008.
- [18] H.J. Zhai, B. Kiran, J. Li, L.S. Wang, Hydrocarbon analogs of boron clusters: planarity, aromaticity, and antiaromaticity, *Nat. Mater.* 2 (2003) 827–833.
- [19] D.Y. Zubarev, A.I. Boldyrev, Comprehensive analysis of chemical bonding in boron clusters, *J. Comput. Chem.* 28 (2007) 251–268.
- [20] Z.A. Piazza, H.S. Hu, W.L. Li, Y.F. Zhao, J. Li, L.S. Wang, Planar hexagonal B36 as a potential basis for extended single-atom layer boron sheets, *Nat. Commun.* 5 (2014) 3113.
- [21] W.L. Li, Q. Chen, W.J. Tian, H. Bai, Y.F. Zhao, H.S. Hu, J. Li, H.J. Zhai, S.D. Li, L. S. Wang, The B35 cluster with a double-hexagonal vacancy: a new and more flexible structural motif for borophene, *J. Am. Chem. Soc.* 136 (2014) 12257–12260.
- [22] A.J. Mannix, X.F. Zhou, B. Kiraly, J.D. Wood, D. Alducin, B.D. Myers, X. Liu, B. L. Fisher, U. Santiago, J.R. Guest, et al., Synthesis of borophenes: anisotropic, two-dimensional boron polymorphs, *Science* 350 (2015) 1513.
- [23] B. Feng, J. Zhang, Q. Zhong, W. Li, S. Li, H. Li, P. Cheng, S. Meng, L. Chen, K. Wu, Experimental realization of two-dimensional boron sheets, *Nat. Chem.* 8 (2016) 563–568.
- [24] S.Y. Xie, Y. Wang, X.B. Li, Flat boron: a new cousin of graphene, *Adv. Mater.* 31 (2019), 1900392.
- [25] Y.V. Kaneti, D.P. Benu, X. Xu, B. Yuliarto, Y. Yamauchi, D. Golberg, Borophene: two-dimensional boron monolayer: synthesis, Properties, and potential applications, *Chem. Rev.* 111 (2022) 1000–1052.
- [26] H.J. Zhai, Y.F. Zhao, W.L. Li, Q. Chen, H. Bai, H.S. Hu, Z.A. Piazza, W.J. Tian, H. G. Lu, Y.B. Wu, Y.W. Mu, G.F. Wei, Z.P. Liu, J. Li, S.D. Li, L.S. Wang, Observation of an all-boron fullerene, *Nat. Chem.* 6 (2014) 727–731.
- [27] N.G. Swacki, A. Sadrzadeh, B.I. Yakobson, B80 fullerene: an ab initio prediction of geometry, stability, and electronic structure, *Phys. Rev. Lett.* 98 (2007), 166804.
- [28] D.L.V.K. Prasad, E.D. Jemmis, Stuffing improves the stability of fullerene-like boron clusters, *Phys. Rev. Lett.* 100 (2008), 165504.
- [29] S. De, A. Willand, M. Amsler, P. Pochet, L. Genovese, S. Goedecker, Energy landscape of fullerene materials: a comparison of boron to boron nitride and carbon, *Phys. Rev. Lett.* 106 (2011), 225502.
- [30] W.J. Chen, Y.Y. Ma, T.T. Chen, M.Z. Ao, D.F. Yuan, Q. Chen, X.X. Tian, Y.W. Mu, S. D. Li, L.S. Wang, B48⁻: a bilayer boron cluster, *Nanoscale* 13 (2021) 3868–3876.
- [31] L. Sai, X. Wu, N. Gao, J. Zhao, R.B. King, Boron clusters with 46, 48, and 50 atoms: competition among the core-shell, bilayer and quasi-planar structures, *Nanoscale* 9 (2017), 13905.
- [32] C. Chen, H. Lv, P. Zhang, Z. Zhuo, Y. Wang, C. Ma, W. Li, X. Wang, B. Feng, P. Cheng, X. Wu, K. Wu, L. Chen, Synthesis of bilayer borophene, *Nat. Chem.* 14 (2022) 25.
- [33] X. Liu, Q. Li, Q. Ruan, M.S. Rahn, B.I. Yakobson, M.C. Hersam, Borophene synthesis beyond the single-atomic-layer limit, *Nat. Mater.* 21 (2022) 35.
- [34] W.L. Li, X. Chen, T. Jian, T.T. Chen, J. Li, L.S. Wang, From planar boron clusters to borophenes and metalloborophenes, *Nat. Rev. Chem.* 1 (2017), 0071.
- [35] J. Barroso, S. Pan, G. Merino, Structural transformations in boron clusters induced by metal doping, *Chem. Soc. Rev.* 51 (2022) 1098–1123.
- [36] C. Romanescu, T.R. Galeev, W.L. Li, A.I. Boldyrev, L.S. Wang, Aromatic metal-centered monocyclic boron rings: Co@B8⁻ and Ru@B9, *Angew. Chem. Int. Ed.* 50 (2011) 9334–9337.
- [37] T.R. Galeev, C. Romanescu, W.L. Li, L.S. Wang, A.I. Boldyrev, Observation of the highest coordination number in planar species: decacoordinated Ta@B10⁻ and Nb@B10⁻ anions, *Angew. Chem. Int. Ed.* 51 (2012) 2101–2105.
- [38] C. Romanescu, T.R. Galeev, W.L. Li, A.I. Boldyrev, L.S. Wang, Transition-metal-centered monocyclic boron wheel clusters (M@Bn): a new class of aromatic borometallic compounds, *Acc. Chem. Res.* 46 (2013) 350–358.
- [39] I.A. Popov, T. Jian, G.V. Lopez, A.I. Boldyrev, L.S. Wang, Cobalt-centred boron molecular drums with the highest coordination number in the CoB16⁻ cluster, *Nat. Commun.* 6 (2015) 8654.
- [40] T. Jian, W.L. Li, I.A. Popov, G.V. Lopez, X. Chen, A.I. Boldyrev, J. Li, L.S. Wang, Manganese-centered tubular boron cluster – MnB16⁻: a new class of transition-metal molecules with high coordination, *J. Chem. Phys.* 144 (2016), 154310.
- [41] W.L. Li, T. Jian, X. Chen, H.R. Li, T.T. Chen, X.M. Luo, S.D. Li, J. Li, L.S. Wang, Ta-doped B20⁻: competition between a B2-Ta@B18 tubular molecular rotor and a 20-membered boron drum, *Chem. Commun.* 53 (2017) 1587–1590.
- [42] W.L. Li, T. Jian, X. Chen, T.T. Chen, G.V. Lopez, J. Li, L.S. Wang, The planar CoB18⁻ cluster as a motif for metalloborophenes, *Angew. Chem. Int. Ed.* 55 (2016) 7358–7363.
- [43] T. Jian, W.L. Li, X. Chen, T.T. Chen, G.V. Lopez, J. Li, L.S. Wang, Competition between drum-like and quasi-planar structures in RhB18⁻: motifs for metalloboronnanotubes or metallo-borophenes, *Chem. Sci.* 7 (2016) 7020–7027.
- [44] A.N. Alexandrova, A.I. Boldyrev, H.J. Zhai, L.S. Wang, Electronic structure, isomerism, and chemical bonding in B7⁻ and B7, *J. Phys. Chem. A* 108 (2004) 3509–3517.
- [45] L.L. Pan, J. Li, L.S. Wang, Low-lying isomers of the B9⁻ boron cluster: the planar molecular wheel versus three-dimensional structures, *J. Chem. Phys.* 129 (2008), 024302.
- [46] A.N. Alexandrova, H.J. Zhai, L.S. Wang, A.I. Boldyrev, Molecular wheel B82⁻ as a new inorganic ligand. Photoelectron spectroscopy and ab initio characterization of LIB8, *Inorg. Chem.* 43 (2004) 3552–3554.
- [47] T.R. Galeev, C. Romanescu, W.L. Li, L.S. Wang, A.I. Boldyrev, Valence isoelectronic substitution in the B8⁻ and B9⁻ molecular wheels by an Al dopant atom: umbrella-like structures of AlB7⁻ and AlB8, *J. Chem. Phys.* 135 (2011), 10430.
- [48] T.T. Chen, W.L. Li, T. Jian, X. Chen, J. Li, L.S. Wang, PrB7⁻: a praseodymium-doped boron cluster with a PrII center coordinated by a doubly aromatic planar η⁷-B73⁻ ligand, *Angew. Chem. Int. Ed.* 56 (2017) 6916–6920.
- [49] W.J. Tian, W.J. Chen, M. Yan, R. Li, Z.H. Wei, T.T. Chen, Q. Chen, H.J. Zhai, S. D. Li, L.S. Wang, Transition-metal-like bonding behaviors of a boron atom in a boron-cluster boronyl complex [η⁷-B7]-B-BO], *Chem. Sci.* 12 (2021) 8157–8164.
- [50] W.L. Li, T.T. Chen, W.J. Chen, J. Li, L.S. Wang, Monovalent lanthanide(I) in borozene complexes, *Nat. Commun.* 12 (2021) 6467.
- [51] W.J. Chen, M. Kulichenko, H.W. Choi, J. Cavanagh, D.F. Yuan, A.I. Boldyrev, L. S. Wang, Photoelectron spectroscopy of size-selected bismuth-boron clusters: BiBn⁻ (n = 6–8), *J. Phys. Chem. A* 125 (2021) 6751–6760.
- [52] W.J. Chen, Y.Y. Zhang, W.L. Li, H.W. Choi, J. Li, L.S. Wang, AuB8⁻: an Au-borozene complex, *Chem. Commun.* 58 (2022) 3134.
- [53] W.L. Li, T.T. Chen, D.H. Xing, X. Chen, J. Li, L.S. Wang, Observation of highly stable and symmetric lanthanide octa-boron inverse sandwich clusters, *Proc. Natl. Acad. Sci. U.S.A.* 115 (2018) E6972–E6977.
- [54] T.T. Chen, W.L. Li, J. Li, L.S. Wang, [La(η⁷-Bx)La]⁻ (x = 7–9): a new class of inverse-sandwich complexes, *Chem. Sci.* 10 (2019) 2534–2542.
- [55] H.J. Zhai, L.S. Wang, D. Yu Zubarev, A.I. Boldyrev, Gold apes hydrogen. The structure and bonding in the planar B7Au2⁻ and B7Au2 clusters, *J. Phys. Chem. A* 110 (2006) 1689–1693.
- [56] Q. Chen, H.J. Zhai, S.D. Li, L.S. Wang, On the structures and bonding in boron-gold alloy clusters: B6Au⁻ and B6Auⁿ (n = 1–3), *J. Chem. Phys.* 138 (2013), 084306.
- [57] Q. Chen, H. Bai, H.J. Zhai, S.D. Li, L.S. Wang, Photoelectron spectroscopy of boron-gold alloy clusters and boron boronyl clusters: B3Au⁻ and B3(BO)n⁻ (n = 1, 2), *J. Chem. Phys.* 139 (2013), 044308.
- [58] L.F. Cheung, J. Czekner, G.S. Kocheil, L.S. Wang, High resolution photoelectron imaging of boron-bismuth binary clusters: Bi2Bn⁻ (n = 2–4), *J. Chem. Phys.* 150 (2019), 064304.
- [59] L. Wen, Q. Li, B. Song, L. Yang, E. Ganz, The evolution of geometric structures, electronic properties, and chemical bonding of small phosphorus-boron clusters, *Condens. Matter* 7 (2022) 36.
- [60] L. Xie, W.L. Li, C. Romanescu, X. Huang, L.S. Wang, A photoelectron spectroscopy and density functional study of di-tantalum boride clusters: Ta2Bx⁻ (x = 2–5), *J. Chem. Phys.* 138 (2013), 034308.
- [61] W.L. Li, L. Xie, T. Jian, C. Romanescu, X. Huang, L.S. Wang, Hexagonal bipyramidal Ta2B6⁻/0 clusters: B6 rings as structural motifs, *Angew. Chem. Int. Ed.* 53 (2014) 1288.
- [62] A.C. Reber, S.N. Khanna, Electronic structure, stability, and oxidation of boron-magnesium clusters and cluster solids, *J. Chem. Phys.* 142 (2015), 054304.

- [63] Y.J. Wang, L.Y. Feng, J.C. Guo, H.J. Zhai, Dynamic Mg₂B₈ Cluster: a nanoscale compass, *Chem. Asian J.* 12 (2017) 2899–2903.
- [64] R. Yu, J. Barroso, M.H. Wang, W.Y. Liang, C. Chen, X. Zarate, M. Orozco Ica, Z. H. Cui, G. Merino, Structure and bonding of molecular stirrers with formula B₇M₂– and B₈M₂ (M = Zn, Cd, Hg), *Phys. Chem. Chem. Phys.* 22 (2020) 12312–12320.
- [65] M. Kulichenko, W.J. Chen, H.W. Choi, D.F. Yuan, A.I. Boldyrev, L.S. Wang, Probing copper-boron interactions in the Cu₂B₈– bimetallic cluster, *J. Vac. Sci. Technol.* 40 (2022), 042201.
- [66] L.S. Wang, H.S. Cheng, J. Fan, Photoelectron spectroscopy of size-selected transition metal clusters: fen–, n = 3–24, *J. Chem. Phys.* 102 (1995) 9480–9493.
- [67] H. Zhai, M.A. Ha, A.N. Alexandrova, AFFCK: adaptive force-field-assisted ab Initio coalescence kick method for global minimum search, *J. Chem. Theor. Comput.* 11 (2015) 2385.
- [68] C. Adamo, V. Barone, Toward reliable density functional methods without adjustable parameters: the PBE0 model, *J. Chem. Phys.* 110 (1999) 6158–6170.
- [69] T.H. Dunning Jr., P.J. Hay, in: H.F. Schaefer (Ed.), *Modern Theoretical Chemistry 3* (1977) 1–28. Plenum, New York.
- [70] W.R. Wadt, P.J. Hay, Ab initio effective core potentials for molecular calculations. Potentials for main group elements Na to Bi, *J. Chem. Phys.* 82 (1985) 284.
- [71] T.H. Dunning, Gaussian basis sets for use in correlated molecular calculations. I. The atoms boron through neon and hydrogen, *J. Chem. Phys.* 90 (1989) 1007–1023.
- [72] N.B. Balabanov, K.A. Peterson, Systematically convergent basis sets for transition metals. I. All-electron correlation consistent basis sets for the 3d elements Sc–Zn, *J. Chem. Phys.* 123 (2005), 064107.
- [73] M.J. Frisch, G.W. Trucks, H.B. Schlegel, G.E. Scuseria, M.A. Robb, J.R. Cheeseman, G. Scalmani, V. Barone, G.A. Petersson, H. Nakatsuji, et al., *Gaussian 16*, Revision C.01, Gaussian, Inc., 2016.
- [74] R. Bauernschmitt, R. Ahlrichs, Stability analysis for solutions of the closed shell Kohn–Sham equation, *J. Chem. Phys.* 104 (1996) 9047–9052.
- [75] D.Y. Zubarev, A.I. Boldyrev, Developing paradigms of chemical bonding: adaptive natural density partitioning, *Phys. Chem. Chem. Phys.* 10 (2008) 5207–5217.
- [76] N.V. Tkachenko, A.I. Boldyrev, Chemical bonding analysis of excited states using the Adaptive Natural Density Partitioning method, *Phys. Chem. Chem. Phys.* 21 (2019) 9590–9596.
- [77] A.I. Boldyrev, L.S. Wang, All-metal aromaticity and antiaromaticity, *Chem. Rev.* 105 (2005) 3716–3757.
- [78] H.J. Zhai, L.S. Wang, A.N. Alexandrova, A.I. Boldyrev, On the electronic structure and chemical bonding of B₅– and B₅ by photoelectron spectroscopy and Ab Initio calculations, *J. Chem. Phys.* 117 (2002) 7917–7924.
- [79] A.N. Alexandrova, A.I. Boldyrev, H.J. Zhai, L.S. Wang, E. Steiner, P.W. Fowler, Structure and bonding in B₆– and B₆: planarity and antiaromaticity, *J. Phys. Chem. A* 107 (2003) 1359–1369.
- [80] L.S. Wang, Covalent gold, *Phys. Chem. Chem. Phys.* 12 (2010) 8694–8705.
- [81] D.Z. Li, Q. Chen, Y.B. Wu, H.G. Lu, D.D. Li, Double-chain planar D_{2h} B₄H₂, D_{2h} B₈H₂, and D_{2h} B₁₂H₂: conjugated aromatic boranes, *Phys. Chem. Chem. Phys.* 14 (2012) 14769–14774.
- [82] H.J. Zhai, Q. Chen, H. Bai, H.G. Lu, W.L. Li, S.D. Li, L.S. Wang, Pi and sigma double conjugations in boronyl polyborane nanoribbons: bn(BO)₂– and Bn(BO)₂ (n = 5–12), *J. Chem. Phys.* 139 (2013), 174301.